Research Article

Average Fracture Energy for Crack Propagation in Postfire Concrete

Kequan Yu, Jiangtao Yu, and Zhoudao Lu

College of Civil Engineering, Tongji University, Shanghai 200092, China

Correspondence should be addressed to Jiangtao Yu; yujiangtao@tongji.edu.cn

Wedge-splitting tests of postfire concrete specimens were carried out in the present research to obtain the load-displacement curves. Ten temperatures varying from room temperature to 600°C were employed. In order to calculate the accurate fracture energy, the tails of load-displacement curves were best fitted using exponential and power functions. Three fracture energy quantities (fracture energy G_F, stable fracture energy G_{FS}, and unstable fracture energy G_{FU}) with their variation tendency and their mutual relationship were determined to predict energy consumption for the complete fracture propagation. Additionally, the stable fracture work W_{FS} was also calculated. All these fracture parameters sustain an increase-decrease tendency which means that the fracture property of postfire concrete shares the same tendency.

1. Introduction

Since the application of fracture mechanics to concrete, the energy consumption for crack propagation in concrete has been a popular topic. For concrete, the specific fracture energy G_F has been proven to be a useful parameter in the structure design and fracture behavior modeling. The specific fracture energy of concrete was defined based on a tensile test as the energy absorbed per unit crack area in widening the crack from zero to or beyond the critical value above which no stress can transmit [1]. Based on the work-of-fracture principle, three-point bending test [2], compact tension [3], and wedge-splitting method [4] were proposed as alternative methods to determine the specific fracture energy G_F. It is computed as the area under the entire imposed load P and load-line displacement curve divided by the projected area of uncracked ligament, so the fracture energy G_F represents the average or nominal energy consumption of concrete for an entire crack propagation process.

The existence of fracture process zone FPZ ahead of a crack is now well accepted. Since the 1970s, it has been known that the evolution of the FPZ undergoes two distinct periods—precritical stable crack growth and unstable fracture process [5]. There is no doubt that crack propagation is accompanied by energy dissipation, and the motive for crack propagation comes from either work provided by the imposed load or released strain energy. Fracture energy is one appropriate consideration to describe the amount of energy consumed during crack propagation process.

It is worth noting that the fracture energy can only represent the amount of average energy dissipation for entire crack propagation from crack initiation to complete failure without characterizing crack stable propagation and unstable fracture periods. So even with G_F, it is still not clear how much energy is dissipated during those two crack extension periods. Xu et al. [6] proposed two new concepts the stable fracture energy G_{FS} and unstable fracture energy G_{FU} to describe fracture responses for different crack propagation periods. It is found that G_{FS} kept constant for different ligament lengths, whereas G_F and G_{FU} showed the apparent size effect. But the accurate calculation of fracture surface remains unsolved. It is known that the true path of crack extension is tortuous, not straight as expected. The projected area underestimates the true fracture area. Hence, these parameters are actually nominal values.

The fracture energy of postfire concrete has been studied by several researchers [7–12]. It is found that the residual fracture energy sustained an increase-decrease tendency with the turning point at approximately 450°C. The increase tendency is due to the energy dissipation of microcracks distributing in

the concrete, whereas the thermal damage induced by high temperatures reduces the residual fracture energy. However, in these researches, the influence of loading-displacement tail was unknown or not considered.

In present paper, wedge-splitting experiments of under ten temperatures levels varying from 20°C to 600°C and the specimens size of 230 mm × 200 mm × 200 mm with initial-notch depth ratios 0.4 are implemented [12]. Based on the work-of-fracture idea, the residual fracture energy G_F is calculated considering the influence of load-displacement tail. Furthermore, the fracture energy consumption for crack stable extension and unstable extension, that is, G_{FS}, G_{FU}, is investigated. However, the true fracture surface remains undetermined and extremely difficult for specimens subjected to high temperatures, so these three fracture energy parameters are still nominal values. Hence, corresponding to G_{FS} and G_{FU}, the stable and unstable fracture work which neglect the fracture surface and their variation about temperatures are thus determined. From these parameters the fracture properties of postfire concrete could be described.

2. Fracture Energies for an Entire Crack Propagation Period

Based on the global energy balance principle, the work performed by a generalized force P on its displacement will be transformed into energy: one part of energy is stored in the body in the form of strain energy and the other part is used for crack propagation. It can be mathematically written as [6]:

$$G_{Fi}A_i = W_i - \Delta U_i = \int_0^{\delta_i} P d\delta - \Delta U_i, \quad (1)$$

where G_{Fi} = average energy needed for unit crack propagation during period from crack initiation to any instant of time i; A_i = newly formed fracture area for this period; the product of these two quantities represents the energy absorbed for crack propagation during this period; W_i = work performed by the external force P during the same period; U_i = increase of elastic strain energy of the body until time i; δ_i = crack opening displacement corresponding to P. If time i is approaching the failure terminal point $i = 1$, where the load drops to zero, then G_{Fi} in (1) will reduce to

$$G_F = \frac{W}{A_{lig}} = \frac{\int_0^{\delta_1} P d\delta}{b(h - a_0)}, \quad (2)$$

where G_F = RILEM fracture energy; W = total energy provided by the external force P for crack propagation; A_{lig} = projected fracture area perpendicular to the tensile stress direction; b = specimen thickness; h = specimen height; a_0 = initial crack length.

During the stable crack propagation period, the load will increase up to its peak value P_{max} with its corresponding displacement reaching COD_c; see Figure 1. So, based
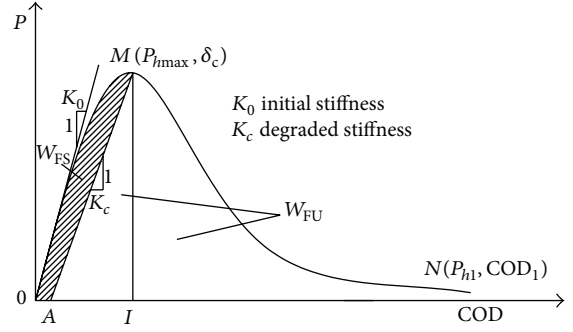

FIGURE 1: Energy consumption for an entire crack propagation period.

on (1), the average energy absorbed during this period can be evaluated by

$$G_{FS} = \frac{W_{FS}}{A_S} = \frac{W_P - \Delta U_S}{A_S} = \frac{W_{OAMO}}{A_S}$$

$$= \frac{W_{OIMO} - W_{AIMA}}{A_S} = \frac{\int_0^{COD_c} P dCOD_c - \Delta U_S}{A_S}, \quad (3)$$

where G_{FS} by naming the stable fracture energy = average energy needed for the crack to grow unit area during the crack stable propagation; A_S = change in fracture area; $W_{FS} = W_{OAMO}$ = energy provided for stable crack propagation as shown in Figure 1 by the shaded area; $W_P = W_{OIMO}$ = work performed by the external force P for crack increases its area A_S; $\Delta U_S = W_{AIMA}$ = increased elastic strain energy of the body; and COD_c = critical crack opening displacement.

From the definition of the stable fracture energy G_{FS}, it is implied that the work from the imposed load P is expended in two forms during the crack stable propagation: one part is stored in the body in the form of the elastic strain energy (ΔU_S) and the other part is the energy absorbed by the fracture zone mainly to counteract the resistance caused by the cohesive forces along the FPZ. In the same way, the unstable fracture energy, denoted by G_{FU}, is defined based on energy equilibrium as

$$G_{FU} = \frac{W_U}{A_U} = \frac{W - W_S}{A_U}, \quad (4)$$

where W_U = energy needed for the crack unstable propagation period and A_U = change in fracture area. During this period, the stored energy is completely released until the deformation reaches its maximum value COD_1 when the load closes to zero. Similar to the RILEM fracture energy G_F, the establishment of the stable fracture energy G_{FS} and unstable fracture energy G_{FU} rests upon the implicit assumption that no other energy consumption occurs outside the fracture zone.
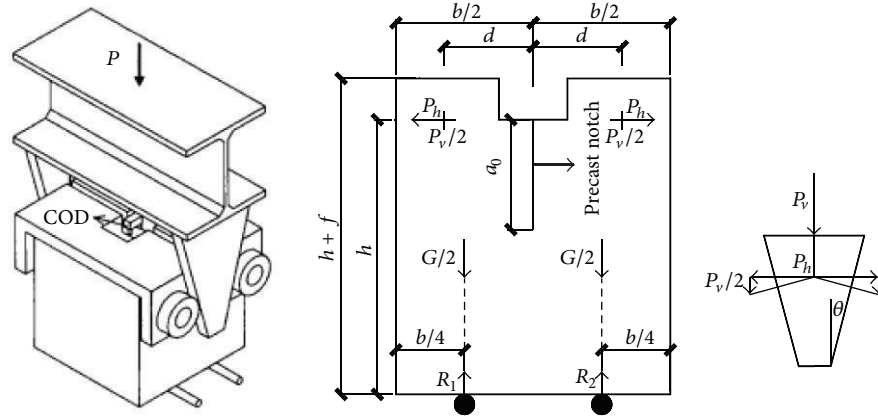
FIGURE 2: Test setup and geometry of specimens.

3. Experimental Program and Experimental Phenomena

In this test, concrete specimens were prepared using an ordinary silicate cement PO. 42.5 produced conforming to the Chinese standard. Coarse aggregate was calcareous crushed stone with a maximum size of 16 mm, and river sand was used as the fine aggregates and its maximum diameter was 5 mm. Details of the mix proportioning (by weight) used for concrete and some mechanical properties are Cement : Sand : Limestone Coarse aggregate : Water : fly ash = 1.00 : 3.44 : 4.39 : 0.80 : 0.26.

Fracture properties of concrete were determined by means of the wedge splitting test [4]. The test setup and geometry of the specimen are schematically represented in Figure 2. Compared to three-point bending notched beams, the wedge-splitting test has following advantages. For the three-point bending beams, inaccurate measurement of load-point displacement and the self-weight of the specimen could influence the real value of the fracture energy. During the test, beams should be carefully handled due to their heavy weight. However, using the WS specimens, the recorded COD in a horizontal plane is not affected by the crushing of the specimen at the supports or some other factors. Besides, the WS specimens are simple and easily prepared in laboratories or on site.

A total of 50 concrete specimens with the same dimensions $230 \times 200 \times 200$ mm were prepared; the geometry of the specimens and the test setup are shown in Figure 2 (b = 200 mm, d = 65 mm, h = 200 mm, f = 30 mm, a_0 = 80 mm, and θ = 15°). All the specimens had a precast notch of 80 mm height and 3 mm thickness, achieved by placing a piece of steel plate into the molds prior to casting. Each wedge splitting specimen was embedded with a thermal couple in the center of specimen for temperature control.

Nine heating temperatures, ranging from 65°C to 600°C (T_m = 65°C, 120°C, 200°C, 300°C, 350°C, 400°C, 450°C, 500°C, and 600°C), were adopted with the ambient temperature as a reference. Because it was recognized that the fracture behavior measurements were generally associated with significant scatter, five repetitions were performed for each temperature.

An electric furnace with net dimensions $300 \times 300 \times 900$ mm was used for heating. When the designated T_m was reached, the furnace was shut down, and the specimens were naturally cooled for 7 days prior to the test. It averagely took 50, 95, 135, 182, 218, 254, 294, 342, and 453 minutes for the specimens to reach the final temperatures, respectively (from 65°C to 600°C). Figure 3 shows the typical temperature history for several cases with different maximum temperatures. After heating, microcracks disperse on the specimen surface, especially for temperatures higher than 200°C (see in Figure 4).

The fracture surfaces at different temperature intervals (20°C, 200°C, 350°C, 450°C, and 600°C) are shown in Figure 5, which became lighter but more tortuous with increasing temperatures.

A universal machine with a maximum capacity of 1000 kN was used to conduct the wedge splitting tests. During the test, the vertically applied load P_v and the crack opening displacement COD along the horizontal load line were simultaneously recorded through a data acquisition system. Referring to Figure 2, the splitting force P_h is actually the horizontal component of the force acting on the bearing. Taking the wedge angle into consideration, its relation with the recorded applied load P_v can be developed based on force equilibrium ignoring the small influence from the friction for different roller bearings:

$$P_h = \frac{P_v}{2 \tan \theta}. \tag{5}$$

To obtain the complete P-COD curves (shown in Figure 6), the test rate was fixed at 0.4 mm/min, such that it took approximately 20 minutes to complete a single test of specimens subjected to less than 300°C and 30 minutes for beyond 300°C.

The fracture of specimen is essentially due to the bending moment caused by the horizontal splitting force P_h, vertical component $1/2P_v$, and self-weight of the specimen. Two
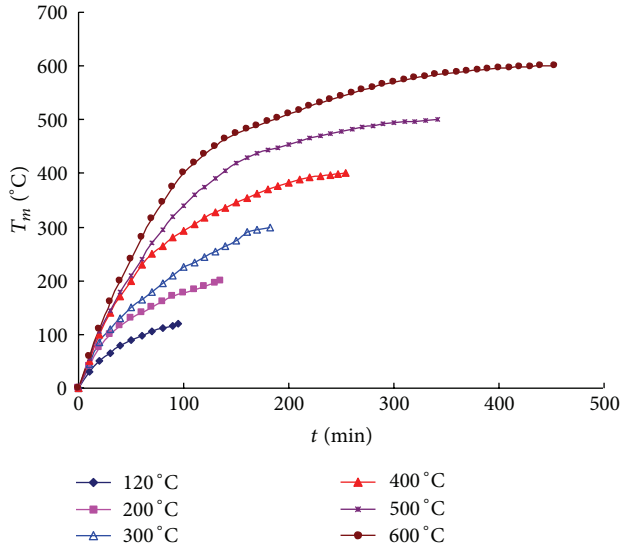
FIGURE 3: Typical temperature history of specimens.

FIGURE 4: Microcracks on specimen surface (600°C).

symmetrical supports are placed below the center of gravity of each half of the specimen. In doing so, the influence of the dead weight of the specimen and part of the vertical component force on the calculation of the fracture energies could be counteracted. Each roll axis is fixed at the same horizon as the lower plane of the groove and is very close to the center of gravity of each half of the specimen in the vertical position (shown in Figure 2). Due to the carefulness in the choice of the specimen geometry, the roll axis location, and the placement of the supports, the horizontal force P_h contributes most to fracturing the specimen. Therefore, P_h-COD curves were directly used in the calculation of the RILEM fracture energy G_F, stable fracture energy G_{FS}, and unstable fracture energy G_{FU}.

For our test results, the P_h-COD curves could be easily obtained from the monitored P_v-COD curves and (5). Figure 6 contains the plots of P_h-COD curves for several temperatures and typical P_v-COD curves for all temperatures.

From Figure 6(a) to 6(c), it is found that with the increasing of temperature (20°C–600°C), the divergence between the curves for the same temperature is more significant. In particular 600°C, the ultimate load P_u of specimen WS50 is one time higher than the one of specimen WS47. Additionally, the whole loading process is not stable for specimens WS49 (a sudden snap-back) due to the thermal damage induced by high temperature. Figure 6(d) shows the typical P-COD curves of all temperatures. The ultimate load P_u decreases significantly with increasing temperatures T_m, whereas the crack mouth opening displacement (COD) increases with T_m. The initial slope of ascending branches decreases with heating temperatures, and the curves become gradually shorter and more extended.

It is found that the ultimate load $P_{h\,\mathrm{max}}$ decreases with the increasing temperatures, whereas the COD_c increases with T_m (Figure 8). The average value of P_u decreases from 9.17 kN at ambient temperature to 7.92 kN at 120°C, 4.29 kN at 300°C, 3.16 kN at 450°C, and finally 1.38 kN at 600°C, with a final drop of 85%. The value of COD_c increases from 0.178 mm at ambient temperature to 0.352 mm at 200°C, 0.901 mm at 400°C, and 1.848 mm at 600°C, nearly 10 times as the ambient value.

4. Experimental Results and Analysis

4.1. Determination of Residual Fracture Energy G_F. In the calculation of RILEM fracture energy G_F, two things should be carefully considered. One thing is that the work done by the self-weight of loading device should be taken into account. In present experiments, the loading device is attached to the testing machine and the P_h-COD curve includes the self-weight; hence the work should not be calculated again. The other concern pertains to the tail part of the P_h-COD curve: the recorded point (P_{h1}, COD_1) is just one point when the experiment stops, not the actual point of when the load drops to zero. Therefore, cutting the load-deflection tail may lead to noticeable inaccuracy in the true value of fracture energy. Thus, to account for these two factors, the actual RILEM fracture energy G_F based on the work-of-fracture method becomes (see Figure 9)

$$G_F = \frac{W}{A_{\mathrm{lig}}} = \frac{W_1 + W_2}{t\,(h - a_0)}, \tag{6}$$

where W_1 = measured work enclosed by the P_h-COD curve until COD = COD_1; A_{lig} = fresh fracture area; W_2 is the work caused by tail effect part. For W_2, curve fitting technology based on Excel software was used to get its approximate value. In previous research from the test results at ambient temperature [13], it was found out that the descending branch of the P_h-COD curve after one-third of the peak load could be well described by power function (the coefficient of determination R^2 for each curve is close to 1). This study indicates that for specimens subject to no more than 120°C, the power function is more accurate; however, for specimens subject to higher temperatures, exponential function is more suitable (see Figure 9).

(a) Fracture surface of 20°C

(b) Fracture surface of 600°C

(c) Fracture surfaces at typical temperatures (20°C, 200°C, 350°C, 450°C, and 600°C)

Figure 5: Fracture surfaces of postfire specimens.

For power function $P_h = \beta \times COD^{-\lambda} \beta$, $\lambda > 0$, where β, λ = constants for fitting curves. And then the unrecorded work W owing to cutting load-deflection tail can be written as

$$W_2 = \int_{COD_1}^{\infty} \beta \times COD^{-\lambda} dCOD = \frac{\beta}{(\lambda - 1) \times COD_1^{\lambda-1}}. \tag{7}$$

For exponential function $P_h = m \times e^{-n \times COD} m$, $n > 0$, where m, n = constants for fitting curves. And then the unrecorded work W owing to cutting load-deflection tail can be written as

$$W_2 = \int_{COD_1}^{\infty} m \times e^{-n \times COD} d\delta = \frac{m}{ne^{n \times COD_1}}. \tag{8}$$

The parameters of β, λ for 20°C~120°C and m, n for 200°C~600°C, and the value of w_1, w_2 is listed in Table 1.

Some necessary test results are tabulated in Table 1, including the maximum value of the horizontal load $P_{h\,max}$ and its corresponding crack opening displacement COD_c, the

endpoint where P_{h1} approaches zero and the crack opening displacement arrives at COD_1, the initial slope of P_h-COD, that is, the initial stiffness K_0, and the modulus of elasticity E.

Hence, the residual fracture energy described by (1) could be calculated. The values are listed in Table 2 and are shown in Figure 10.

Though the residual fracture energy at each temperature has significant scatter, Figure 10 shows that the average values sustain an increase-decrease tendency with T_m. From 20°C to 450°C, average G_F increases from 339.3 Nm^{-1} to 609 Nm^{-1}, while the temperature reaches 600°C and the fracture energy falls back to 307.8 Nm^{-1}. The detailed explanation would be seen elsewhere [12].

4.2. Determination of Stable Fracture Energy G_{FS} and Unstable Fracture Energy G_{FU}.

As an extension of fracture energy G_F, two other energy-based fracture characteristics, the stable fracture energy G_{FS} and unstable fracture energy G_{FU}, are proposed to describe fracture responses for different crack propagation periods. The analysis shows that fracture energy G_F is actually the weighed average of G_{FS} and G_{FU}, and G_{FS}

(a) P_h versus COD curves of specimens at 120°C

(b) P_h versus COD curves of specimens at 450°C

(c) P_h versus COD curves of specimens at 600°C

(d) Typical P_v versus COD curves of specimens at all temperatures
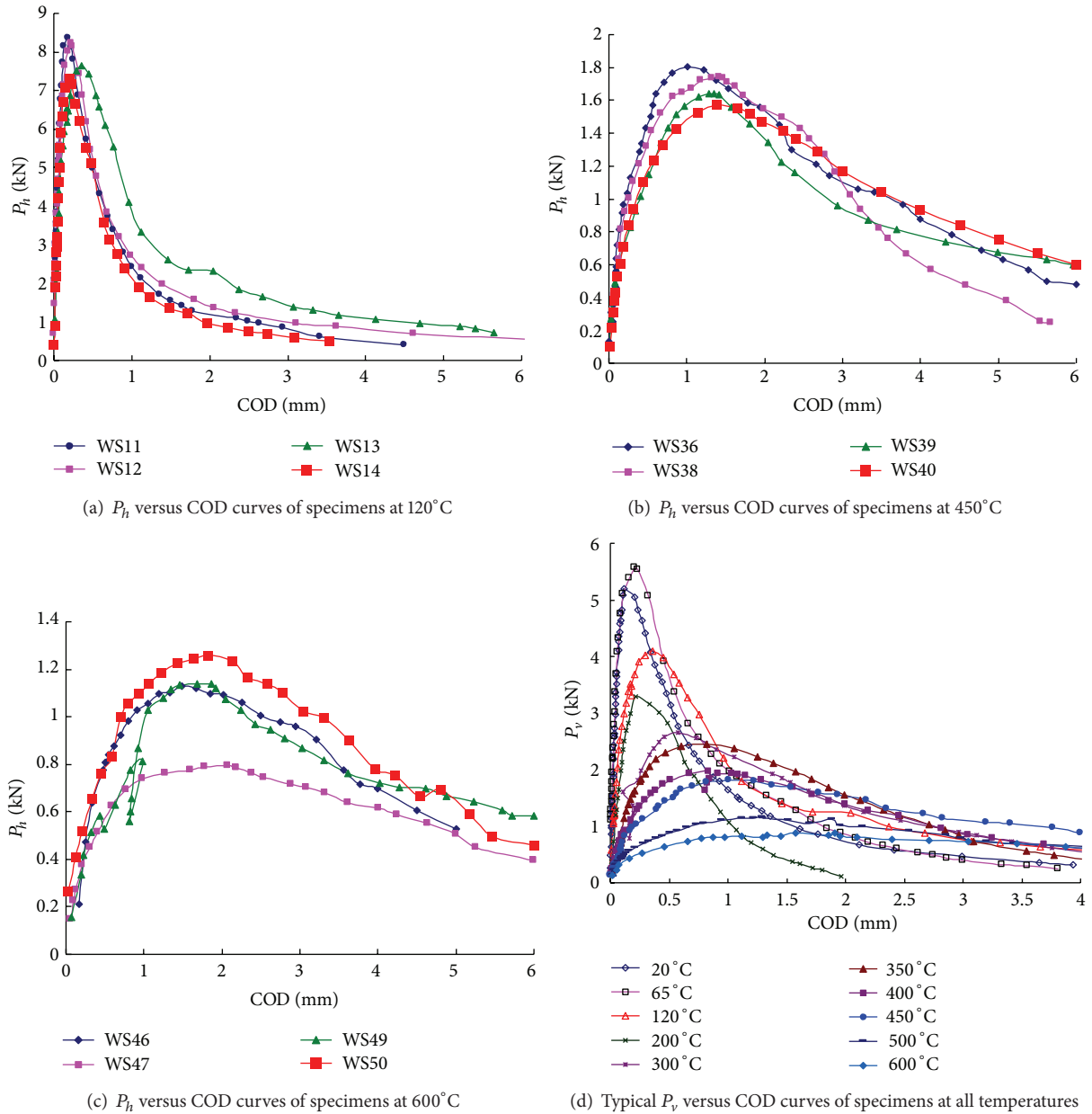
FIGURE 6: P versus CMOD curves of specimens with temperatures.

and G_{FU} could be regarded as two components of G_F. This is very helpful in understanding the whole crack propagation process from the aspect of energy consumption.

To obtain the values of G_{FS} and G_{FU}, the critical effective crack length a_c should first be determined for the calculation of the fracture areas A_S and A_U. Herein, the value a_c was computed based on the double-K fracture model [14]:

$$a = (h + h_0) \left\{ 1 - \left(\frac{13.18}{E \cdot b \cdot c + 9.16} \right)^{1/2} \right\} - h_0, \quad (9)$$

where $c = \text{COD}/P$ is the compliance of specimens, E is modulus of elasticity, b is specimen thickness, h is specimen

height, and h_0 is the thickness of the clip gauge holder. For calculation of critical value of equivalent elastic crack length a_c, the value of crack mouth opening displacement (COD) and P are taken as COD_c and $P_{h\,\text{max}}$, respectively. Equation (9) is valid for 0.2–0.8 within 2% accuracy. The value of a_c is reported in Table 1.

In a typical load-displacement curve shown in Figure 1, K_0 is the initial stiffness of the load-displacement curve before the start of the fracture process. At critical state when the load arrives at its peak value P_{max} and its corresponding displacement reaches COD_c, the stiffness K_c may not be the same as the initial K_0. The degradation of stiffness is the result of crack propagation. To make it simple, here, the value

Table 1: Parameters calculated from wedge-splitting test.

Specimen	Temperature	$P_{h\max}$ (kN)	E (GPa)	a_c (mm)	β/m	λ/n	R^2	W_1	W_2	COD_c (mm)	COD_1 (mm)	K_0 (kN/mm)	K_c (kN/mm)
WS1		8.304	15.30	0.107	1.484	2.273	0.970	5.231	0.389	0.174	1.926	87.081	79.219
WS2		9.407	20.51	0.097	3.131	1.206	0.998	10.468	1.140	0.205	4.914	116.710	113.648
WS3	20°C	10.379	20.66	0.114	2.464	1.117	0.991	8.699	1.818	0.195	3.280	117.610	110.633
WS4		7.884	18.88	0.112	1.599	3.224	0.964	5.128	0.137	0.152	1.903	107.480	98.911
WS5		9.364	15.45	0.107	2.048	1.683	0.991	6.970	0.735	0.199	2.657	87.940	80.103
Average		9.068	18.16	0.107	—	—	0.983	7.299	0.844	0.185	2.936	103.364	96.503
WS6		11.282	21.73	0.113	2.781	1.506	0.996	9.238	0.984	0.195	3.205	123.690	116.172
WS7		8.151	24.79	0.132	2.739	0.987	0.999	10.320	1.263	0.215	6.072	141.100	136.109
WS8	65°C	10.379	19.43	0.115	6.114	1.992	0.954	11.004	0.702	0.212	4.549	110.560	105.418
WS9		10.681	23.25	0.119	2.658	1.030	0.993	9.283	2.250	0.164	3.535	132.330	124.685
WS10		11.610	16.60	0.107	3.185	1.252	0.983	11.466	1.071	0.190	5.324	94.490	90.418
Average		10.421	21.16	0.117	—	—	0.985	10.262	1.254	0.195	4.537	120.434	114.560
WS11		8.353	10.65	0.095	2.477	1.085	0.990	8.423	1.094	0.191	3.418	60.638	57.254
WS12		8.226	11.87	0.107	2.667	0.890	0.999	10.624	1.803	0.224	6.443	67.564	65.212
WS13	120°C	7.631	9.48	0.119	4.340	0.998	0.980	13.227	2.487	0.357	5.641	53.926	50.511
WS14		7.302	15.42	0.117	2.139	1.153	0.998	6.934	1.357	0.198	3.534	87.758	82.839
WS15		—	—	—	—	—	—	—	—	—	—	—	—
Average		7.878	11.85	0.109	—	—	0.992	9.802	1.685	0.243	4.759	67.472	63.954
WS16		—	—	—	—	—	—	—	—	—	—	—	—
WS17		6.466	11.58	0.127	2.266	1.526	0.952	6.260	0.520	0.284	2.558	65.913	57.759
WS18	200°C	5.884	6.98	0.115	2.268	2.982	0.995	5.035	0.129	0.335	1.968	39.732	32.967
WS19		5.071	9.17	0.127	2.770	2.087	0.969	5.397	0.265	0.306	2.786	52.178	46.456
WS20		5.228	7.00	0.130	2.530	0.366	0.903	7.605	1.250	0.458	4.447	39.866	35.765
Average		5.662	8.68	0.125	—	—	0.955	6.074	0.541	0.346	2.940	49.422	43.237
WS21		3.341	2.45	0.121	4.023	0.361	0.981	10.019	0.491	0.792	3.101	13.939	11.004
WS22		5.513	3.49	0.117	4.090	0.300	0.987	13.570	1.105	0.667	5.065	19.869	17.251
WS23	300°C	3.371	1.91	0.113	6.985	0.610	0.982	7.727	0.475	0.672	4.957	10.854	9.384
WS24		4.761	1.99	0.105	4.285	0.345	0.990	12.552	0.987	0.728	6.816	11.350	10.138
WS25		4.076	4.03	0.137	2.172	0.206	0.963	11.532	1.667	0.869	6.874	22.960	20.438
Average		4.213	2.78	0.119	—	—	0.981	11.080	0.945	0.746	5.363	15.794	13.643
WS26		5.701	6.05	0.131	5.702	0.447	0.995	12.290	1.475	0.599	4.549	34.409	29.878
WS27		3.840	2.03	0.125	6.245	0.335	0.958	14.150	1.490	1.003	6.768	11.538	9.829
WS28	350°C	4.718	3.60	0.131	5.553	0.454	0.997	11.312	1.107	0.815	4.053	13.490	16.360
WS29		4.554	3.38	0.130	9.025	0.608	0.995	11.635	0.355	0.821	5.940	19.240	16.582
WS30		3.931	3.21	0.134	7.135	0.532	0.990	10.251	0.654	0.832	5.335	18.279	15.427
Average		4.549	3.65	0.130	—	—	0.987	11.927	1.016	0.814	5.329	19.391	17.615
WS31		3.584	2.56	0.136	3.934	0.307	0.999	11.737	1.033	0.921	6.937	14.557	12.391
WS32		3.039	1.42	0.126	21.138	0.828	0.992	9.300	0.226	0.904	5.614	8.084	6.331
WS33	400°C	3.228	2.12	0.114	2.100	0.224	0.995	8.533	1.575	0.842	5.819	7.348	6.419
WS34		4.476	1.71	0.111	4.208	0.322	0.929	13.388	0.986	0.985	5.940	12.035	8.463
WS35		—	—	—	—	—	—	—	—	—	—	—	—
Average		3.582	1.95	0.122	—	—	0.979	10.740	0.955	0.913	6.078	10.506	8.401

TABLE 1: Continued.

Specimen	Temperature	$P_{h\max}$ (kN)	E (GPa)	a_c (mm)	β/m	λ/n	R^2	W_1	W_2	COD_c (mm)	COD_1 (mm)	K_0 (kN/mm)	K_c (kN/mm)
WS36		3.336	1.41	0.125	5.280	0.299	0.977	13.124	1.553	1.224	5.625	8.037	6.289
WS37		—	—	—	—	—	—	—	—	—	—	—	—
WS38	450°C	3.118	1.46	0.123	10.235	0.543	0.981	10.601	0.978	1.057	5.672	8.291	6.216
WS39		3.056	1.34	0.127	2.518	0.137	0.995	11.955	3.960	1.281	6.784	7.611	6.099
WS40		2.935	1.58	0.137	4.328	0.226	0.998	13.896	2.395	1.394	6.000	8.988	6.900
Average		3.111	1.45	0.128	—	—	0.988	12.394	1.663	1.239	6.020	8.232	6.376
WS41		—	—	—	—	—	—	—	—	—	—	—	—
WS42		2.153	1.76	0.146	3.056	0.245	0.976	7.762	3.054	1.284	5.153	7.251	7.506
WS43	500°C	2.857	1.09	0.119	3.648	0.306	0.979	10.092	1.342	1.174	6.533	6.179	5.069
WS44		1.929	0.75	0.109	2.234	0.153	0.968	8.758	4.119	1.225	6.591	4.243	3.651
WS45		1.838	1.48	0.147	2.300	0.186	0.996	7.826	3.012	1.354	6.225	6.078	6.591
Average		2.194	1.27	0.130	—	—	0.977	8.002	2.494	1.259	6.125	5.938	5.704
WS46		1.129	0.47	0.130	2.102	0.278	0.931	4.197	1.280	1.482	7.000	2.656	2.094
WS47		1.474	0.48	0.128	3.018	0.238	0.954	7.245	2.236	1.784	10.000	2.718	2.233
WS48	600°C	1.649	1.14	0.152	1.992	0.132	0.979	8.390	4.551	1.908	7.100	3.909	2.858
WS49		1.138	0.38	0.131	1.183	0.120	0.971	5.018	2.950	1.865	10.000	1.165	1.761
WS50		1.243	0.38	0.124	2.507	0.285	0.943	5.273	1.280	1.644	8.000	1.174	1.727
Average		1.326	0.57	0.133	—	—	0.956	6.025	2.460	1.737	8.420	2.324	2.135
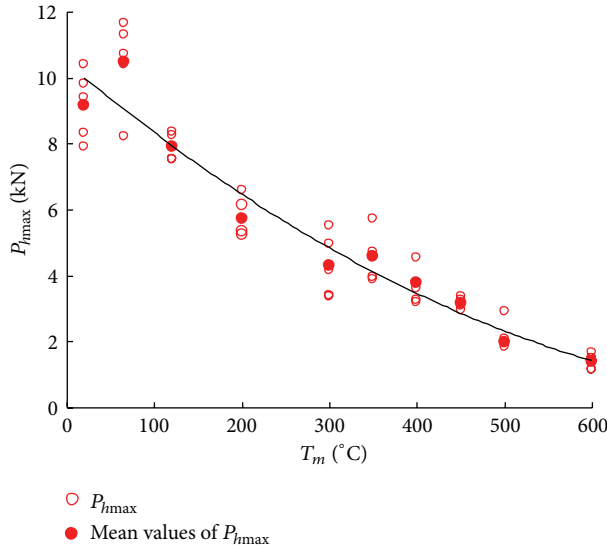
FIGURE 7: Variation tendency of $P_{h\max}$ with T_m.
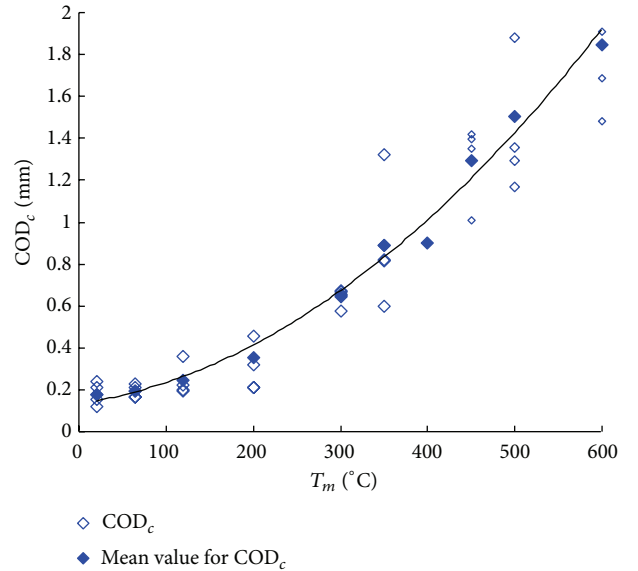
FIGURE 8: Variation tendency of COD_c with T_m.

of K at any value of displacement is assumed to be linear with increased deformation [15].

$$K = \frac{K_0 \left(COD_1 - COD\right)}{\left(COD_1 - COD_0\right)}, \quad (10)$$

where COD_1 = final deformation when the load P approaches zero and COD_0 = displacement before which the stiffness is still kept at K_0. At the origin of P-COD curve, the initial tangent stiffness is K_0. The stiffness becomes degraded beyond the origin point; hence COD_0 is presumed to be zero. It is clear from (10) that $K = K_0$ when $COD = 0$ and

$K = 0$ when $= COD_1$, and K is assumed to be a linear function with respect to the displacement. With the crack opening displacement $COD = COD_c$, the stiffness K_c at this point could approximately be obtained through (10). Note that P-COD is a general term for load-displacement; in our case, the load is the horizontal force P_h and its corresponding displacement is the COD. Therefore, with K_0, COD_1, and COD_c, the approximate degraded stiffness K_c can be gained from (10) and the result is shown in Table 1. Figure 11 shows that the values of stiffness K_c decrease monotonously with temperature due to the thermal damage induced by high temperatures.

TABLE 2: Fracture energies for crack propagation.

Specimen	Temperature	W_0 (Nm)	A_{lig} (m^2)	G_F (Nm^{-1})	W_{OIMA} (Nm)	W_{AIMA} (Nm)	W_{FS} (Nm)	A_{FS} (m^2)	G_{FS} (Nm^{-1})	W_{FU} (Nm)	A_{FU} (m^2)	G_{FU} (Nm^{-1})
WS1		5.620		234.147	1.217	0.407	0.810	0.005	152.502	4.809	0.019	257.361
WS2		11.608		483.664	1.575	0.388	1.187	0.003	350.795	10.421	0.021	504.972
WS3	20°C	10.517	0.024	438.217	2.124	0.470	1.654	0.007	242.557	8.863	0.017	515.877
WS4		5.265		219.394	0.994	0.314	0.680	0.006	107.537	4.586	0.018	259.384
WS5		7.705		321.055	1.693	0.525	1.169	0.005	212.824	6.536	0.019	353.175
Average		8.143		339.295	1.521	0.421	1.100	0.005	213.243	7.043	0.019	378.154
WS6		7.666		425.907	1.791	0.535	1.255	0.007	281.835	6.411	0.017	480.239
WS7		8.687		482.619	1.076	0.241	0.835	0.010	113.926	7.852	0.014	768.132
WS8	65°C	8.779	0.024	487.745	1.475	0.509	0.966	0.007	208.612	7.813	0.017	602.385
WS9		8.649		480.507	1.027	0.440	0.587	0.008	118.113	8.062	0.016	656.640
WS10		9.402		522.360	1.419	0.733	0.686	0.005	210.596	8.716	0.019	614.693
Average		8.637		479.828	1.357	0.492	0.866	0.007	186.616	7.771	0.017	624.418
WS11		7.137		396.516	1.335	0.588	0.746	0.003	251.423	6.391	0.021	416.985
WS12		9.321		517.822	1.475	0.511	0.964	0.005	178.684	8.357	0.019	616.201
WS13	120°C	11.785	0.024	654.732	2.079	0.560	1.520	0.008	193.937	10.266	0.016	878.097
WS14		6.218		345.463	1.044	0.312	0.732	0.007	98.944	5.486	0.017	455.357
WS15		—		—	—	—	—	—	—	—	—	—
Average		8.615		478.633	1.483	0.493	0.991	0.006	180.747	7.625	0.018	591.660
WS16		—		—	—	—	—	—	—	—	—	—
WS17		6.780		282.509	1.522	0.345	1.176	0.009	123.021	5.604	0.015	385.812
WS18	200°C	5.163	0.024	215.135	1.556	0.525	1.031	0.007	146.955	4.132	0.017	243.300
WS19		5.662		235.913	1.252	0.270	0.982	0.009	104.764	4.680	0.015	320.014
WS20		8.854		368.937	1.828	0.365	1.463	0.010	145.364	7.391	0.014	530.467
Average		6.615		275.624	1.540	0.376	1.163	0.009	130.026	5.452	0.015	369.898
WS21		10.510		437.920	2.005	0.439	1.566	0.008	188.640	8.944	0.016	568.895
WS22		14.675		611.467	3.546	0.820	2.726	0.007	364.621	11.949	0.017	723.160
WS23	300°C	8.202	0.024	341.770	2.048	0.579	1.469	0.007	220.394	6.733	0.017	388.453
WS24		13.539		564.120	3.065	1.081	1.984	0.005	404.514	11.555	0.019	605.107
WS25		13.200		549.990	2.552	0.389	2.163	0.011	190.295	11.037	0.013	870.055
Average		12.025		501.053	2.643	0.662	1.982	0.008	273.693	10.044	0.016	631.134
WS26		13.765		573.540	2.689	0.511	2.179	0.010	211.652	11.586	0.014	845.346
WS27		15.639		651.638	2.589	0.703	1.887	0.009	207.566	13.753	0.015	922.314
WS28	350°C	12.420	0.024	517.489	3.827	0.919	2.908	0.010	317.145	9.512	0.014	664.527
WS29		11.990		499.602	2.900	0.611	2.289	0.010	228.349	9.701	0.014	694.230
WS30		10.905		454.375	2.796	0.475	2.320	0.011	216.312	8.585	0.013	646.739
Average		12.944		539.329	2.960	0.644	2.317	0.010	236.205	10.627	0.014	754.631
WS31		12.770		532.090	2.240	0.484	1.756	0.011	156.074	11.014	0.013	860.665
WS32		9.526		396.932	2.678	0.656	2.022	0.009	207.133	7.504	0.015	516.314
WS33	400°C	10.109	0.024	421.188	2.411	0.760	1.651	0.007	242.302	8.457	0.017	491.692
WS34		14.374		598.926	3.638	0.918	2.720	0.006	401.879	11.654	0.018	668.062
WS35		—		—	—	—	—	—	—	—	—	—
Average		11.695		487.284	2.742	0.705	2.037	0.008	251.847	9.658	0.016	634.184

TABLE 2: Continued.

Specimen	Temperature	W_0 (Nm)	A_{lig} (m²)	G_F (Nm⁻¹)	W_{OIMA} (Nm)	W_{AIMA} (Nm)	W_{FS} (Nm)	A_{FS} (m²)	G_{FS} (Nm⁻¹)	W_{FU} (Nm)	A_{FU} (m²)	G_{FU} (Nm⁻¹)
WS36		14.677		611.530	3.255	0.779	2.477	0.009	277.088	12.200	0.015	809.983
WS37		—		—	—	—	—	—	—	—	—	—
WS38	450°C	11.579	0.024	482.451	3.284	0.669	2.615	0.009	303.750	8.964	0.015	582.382
WS39		15.914		663.097	3.281	0.704	2.578	0.009	272.015	13.337	0.015	918.284
WS40		16.291		678.790	3.847	0.532	3.315	0.011	292.743	12.976	0.013	1023.630
Average		14.057		608.967	3.417	0.671	2.746	0.010	286.399	11.869	0.014	833.570
WS41		—		—	—	—	—	—	—	—	—	—
WS42		10.816		450.668	2.080	0.355	1.725	0.013	138.244	9.091	0.011	831.501
WS43	500°C	11.434	0.024	476.413	2.890	0.743	2.146	0.008	272.496	9.288	0.016	576.031
WS44		12.877		536.544	1.495	0.475	1.021	0.006	170.514	11.856	0.018	652.188
WS45		10.838		451.571	2.720	0.308	2.412	0.013	186.562	8.426	0.011	785.892
Average		10.496		478.799	2.296	0.470	1.826	0.010	191.954	9.665	0.014	711.403
WS46		5.477		228.226	1.404	0.287	1.117	0.010	110.974	4.361	0.014	312.890
WS47		9.481		395.057	2.526	0.460	2.066	0.010	213.423	7.415	0.014	517.849
WS48	600°C	12.941	0.024	539.225	2.621	0.389	2.232	0.014	155.808	10.709	0.010	1107.140
WS49		7.968		331.988	1.514	0.635	0.879	0.010	115.238	7.088	0.014	491.494
WS50		6.554		273.074	1.749	0.773	0.976	0.009	151.878	5.578	0.015	342.831
Average		8.484		353.514	1.963	0.509	1.454	0.011	149.464	7.030	0.013	632.922

The stable fracture energy G_{FS} and unstable fracture energy G_{FU} can be derived by following (11)~(13). The specific values of G_{FS} and G_{FU} are compiled in Table 2:

$$G_{\text{FS}} = \frac{W_{\text{FS}}}{A_S} = \frac{W_{\text{OAMO}}}{A_S} = \frac{W_{\text{OIMO}} - W_{\text{AIMA}}}{A_S},$$

$$G_{\text{FU}} = \frac{W_U}{A_U} = \frac{W - W_{\text{FS}}}{A_U}, \tag{11}$$

$$A_S = B(a_c - a_0), \qquad A_U = B(h - a_c), \tag{12}$$

$$W_{\text{AIMA}} = \frac{0.5 P_{h\max}^2}{K_c}. \tag{13}$$

Figure 12 shows the variation of stable fracture energy G_{FS} with temperatures. Similar to the residual fracture energy G_F, it also keeps an increase-decrease tendency with temperatures. Temperatures less than 120°C appear not to induce much thermal damage to concrete, so the cracking resistance almost keeps constant. The values of stable fracture energy G_{FS} at these temperatures are 213 Nm⁻¹, 186 Nm⁻¹, and 180 Nm⁻¹, respectively. The fracture surfaces tend to be more tortuous between 200°C and 450°C than those observed at lower temperatures (see Figure 4) and there exist several cracks competing to form the final fracture, so more energy was dissipated in these specimens. Additionally, the opening of microcracks on the surface and inside the specimens also dissipates energy (see Figure 3). Finally, higher heating temperatures would cause more micro cracks, dehydration, and decomposition and would degrade the resistance. After 450°C, cracking resistance continuously decreases with T_m.

Table 2 shows that the unstable fracture G_{FU} also sustains an increase-decrease tendency with T_m, and its value is much larger than stable fracture energy. Two reasons for larger values of G_{FU} are provided [5]. First, energy consumption besides the main fracture zone takes places for the whole fracture process. During the unstable fracture process, the energy consumption for plasticity or other nonlinear deformation beyond the main FPZ would be much higher, especially for specimens subjected to high temperatures. The other possible reason lies in the calculation of true fracture area. It is known that the interface (transition zone) between cement and aggregate is the weak link in microstructure for normal concrete, and crack propagation would proceed in the path where the energy needs are least. So the true path of crack extension is tortuous and the higher the temperature is, the more tortuous the fracture surface is (see Figure 4), not straight as expected. The projected area is used in the calculation of fracturing surface A_S or A_U, which underestimates the true fracture area. Since the crack experiences much longer distance for the unstable extension, which leads to a greater underestimation of the calculation of the newly fractured area A_U, the calculated G_{FU} is overestimated.

Moreover, in view of (11) and (12), another expression for the fracture energy G_F with respect to G_{FS} and G_{FU} can be followed:

$$G_F = \frac{W}{A} = \frac{G_{\text{FS}} A_S + G_{\text{FU}} A_U}{A} = G_{\text{FS}} \cdot \frac{A_S}{A} + G_{\text{FU}} \cdot \frac{A_U}{A}. \tag{14}$$

Since $A_S + A_U = A$, the fracture energy G_F is the weighed average of G_{FS} and G_{FU}. However, for engineering application, the stable crack propagation is considered to be more

$$y = 2.4636x^{-1.1171}$$
$$R^2 = 0.9929$$
$$y = 4.8054e^{-0.6577x}$$
$$R^2 = 0.9412$$

(a) Curve fitting for specimen of ambient temperature

$$y = 4.0899e^{-0.3001x}$$
$$R^2 = 0.9796$$
$$y = 6.1223x^{-1.1811}$$
$$R^2 = 0.9685$$

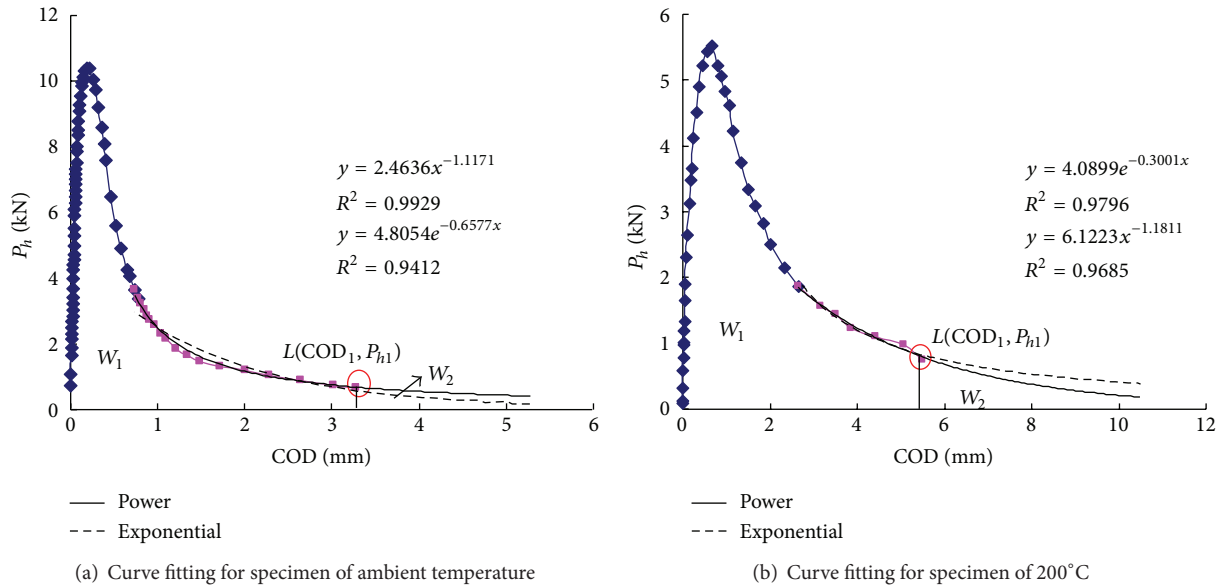(b) Curve fitting for specimen of 200°C

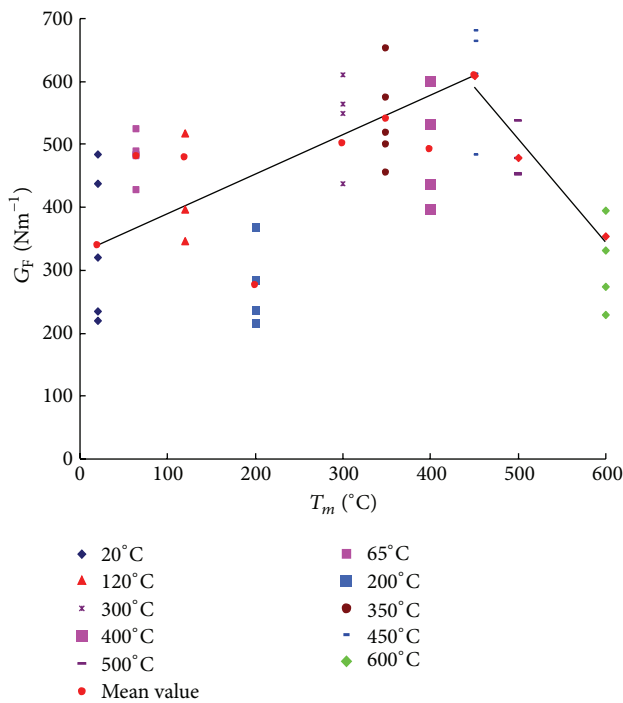FIGURE 9: P-CMOD tail curve fitting of specimens.

FIGURE 10: Residual fracture energy with T_m.
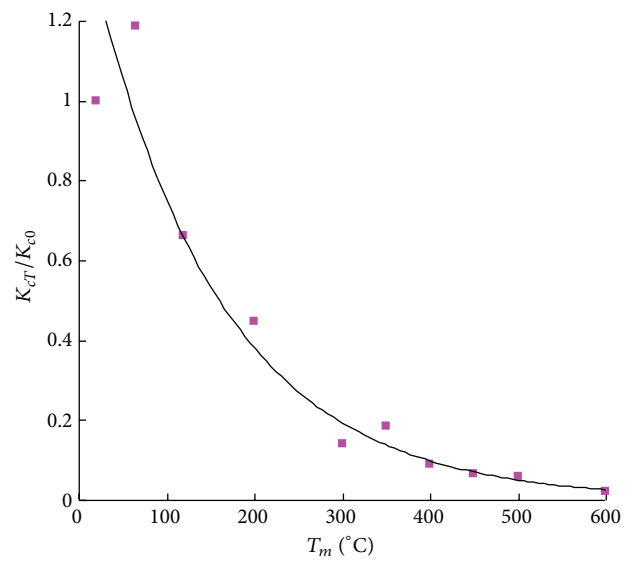
FIGURE 11: Stiffness K_c with T_m.

important, because when the load exceeds the maximum value the whole structure would be in an unstable situation. Hence from Figures 7 and 9, it is concluded that the fracture property of postfire concrete sustains an increase-decrease tendency to 600°C, with a turning point at 450°C.

Furthermore, as mentioned above, the fracture surfaces of A, A_S, A_U are project areas, so G_F, G_{FS}, G_{FU} are nominal fracture energies. To avoid the violence of fracture surface, the variation tendency of stable fracture work W_{FS} is determined

(see Figure 10). Similarly, W_{FS} also keeps an increase-decrease tendency at the same turning temperature of 450°C.

5. Conclusions

Energy consumption during an entire crack propagation period has been investigated, including the fracture energy G_F, stable fracture energy G_{FS}, unstable fracture energy G_{FU}, and stable fracture work W_{FS}. The conclusions are as follows.

(1) Wedge-splitting tests of ten temperatures levels varying from room temperature to 600°C and the specimen size of 230 mm × 200 mm × 200 mm with initial-notch depth ratios 0.4 have been presented. Complete P-COD curves and the curve tails are obtained using
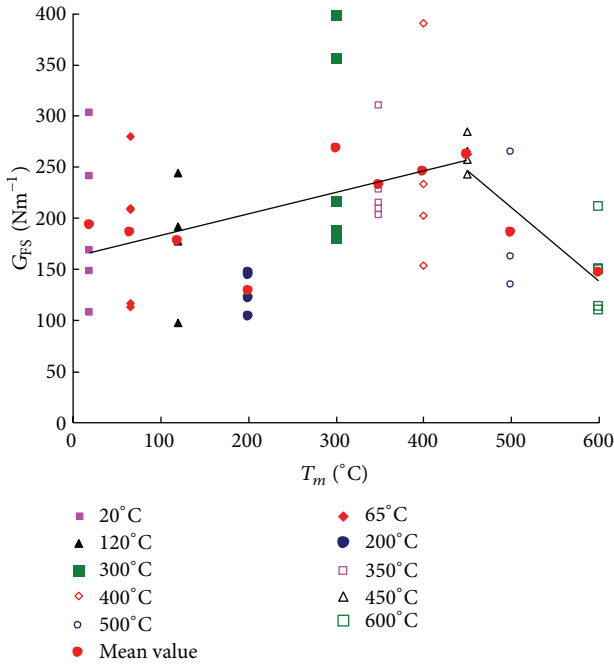
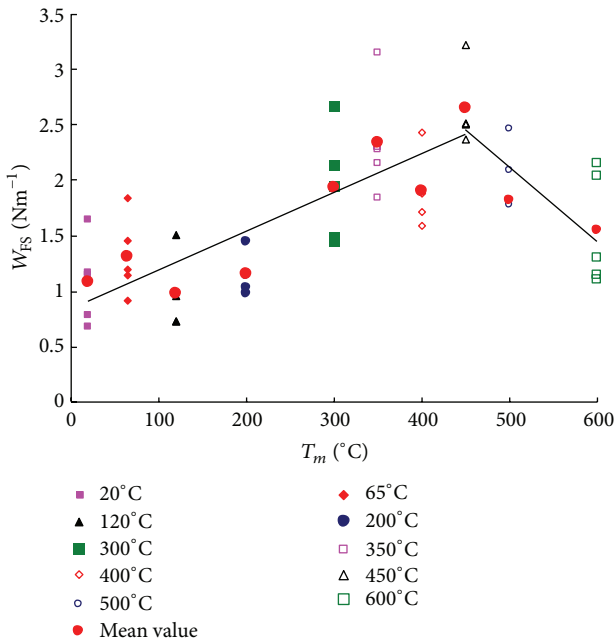FIGURE 12: Stable fracture energy with T_m.

FIGURE 13: Stable fracture work with T_m.

average energy absorption during crack stable propagation, and G_{FU} is used to characterize the average energy consumption for crack unstable propagation and a higher value of G_{FU} than G_{FS} is observed. G_F is actually the weighed average of G_{FS} and G_{FU}.

(3) However, for engineering applications, the stable crack propagation is considered to be more important. From the wedge-splitting tests of different temperatures, it is concluded that G_F, G_{FS} sustain an increase-decrease tendency to 600°C, with a turning point at 450°C. Furthermore, the variation of stable fracture work W_{FS} is determined and shares the same tendency with G_F and G_{FS} (Figure 13). All these three parameters mean that the fracture property of postfire concrete sustains an increase-decrease tendency.

Acknowledgments

References

[1] A. Hillerborg, "The theoretical basis of a method to determine the fracture energy G_F of concrete," *Materials and Structures*, vol. 18, no. 4, pp. 291–296, 1985.

[2] RILEM-Draft-Recommendation (50-FCM) (RILEM), "Determination of the fracture energy of mortar and concrete by means of three-point bend tests on notched beams," *RILEM Materials and Structures*, vol. 18, no. 4, pp. 285–290, 1985.

[3] ASTM International Standard E399-06, "Standard test method for linear-elastic method plane-strain fracture toughness K_{IC} of Metallic Materials," 2006.

[4] E. Brühwiler and F. H. Wittmann, "The wedge splitting test, a new method of performing stable fracture mechanics tests," *Engineering Fracture Mechanics*, vol. 35, no. 1–3, pp. 117–125, 1990.

[5] S. Xu and H. W. Reinhardt, "Determination of double-K criterion for crack propagation in quasi-brittle fracture, Part I: experimental investigation of crack propagation," *International Journal of Fracture*, vol. 98, no. 2, pp. 111–149, 1999.

[6] S. Xu, Y. Zhao, and Z. Wu, "Study on the average fracture energy for crack propagation in concrete," *Journal of Materials in Civil Engineering*, vol. 18, no. 6, pp. 817–824, 2006.

[7] Z. P. Bazand and P. C. Prat, "Effect of temperatures and humidity on fracture energy of concrete," *ACI Materials Journal*, vol. 85, no. 4, pp. 262–271, 1988.

[8] G. Baker, "The effect of exposure to elevated temperatures on the fracture energy of plain concrete," *Materials and Structures*, vol. 29, no. 190, pp. 383–388, 1996.

[9] B. Zhang, N. Bicanic, C. J. Pearce, and G. Balabanic, "Residual fracture properties of normal- and high-strength concrete subject to elevated temperatures," *Magazine of Concrete Research*, vol. 52, no. 2, pp. 123–136, 2000.

[10] C. V. Nielsen and N. Bićanić, "Residual fracture energy of high-performance and normal concrete subject to high temperatures," *Materials and Structures*, vol. 36, no. 262, pp. 515–521, 2003.

exponential and power functions. For specimens subject to no more than 120°C, the power function is more accurate; for higher temperatures, exponential function is more suitable.

(2) Three fracture energy quantities corresponding to different aspects of fracture are proposed. The fracture energy G_F in a general case only represents the average energy dissipation for an entire crack propagation process. G_{FS}, the stable fracture energy, denotes the

[11] B. Zhang and N. Bicanic, "Fracture energy of high-performance concrete at high temperatures up to 450°C: the effects of heating temperatures and testing conditions (hot and cold)," *Magazine of Concrete Research*, vol. 58, no. 5, pp. 277–288, 2006.

[12] J. Yu, K. Yu, and Z. Lu, "Residual fracture properties of concrete subjected to elevated temperatures," *Materials and Structures*, vol. 45, no. 8, pp. 1155–1165, 2012.

[13] Y. H. Zhao, *The analytical study on the energy in the fracture process of concrete [Ph.D. thesis]*, Dalian University of Technology, Dalian, China, 2002.

[14] S. Xu and H. W. Reinhardt, "Crack extension resistance and fracture properties of quasi-brittle softening materials like concrete based on the complete process of fracture," *International Journal of Fracture*, vol. 92, no. 1, pp. 71–99, 1998.

[15] R. K. Navalurkar, C. T. Hsu, S. K. Kim, and M. Wecharatana, "True fracture energy of concrete," *ACI Materials Journal*, vol. 96, no. 2, pp. 213–225, 1999.

Journal of
Nanotechnology

International Journal of
Corrosion

International Journal of
Polymer Science

Smart Materials
Research

Journal of
Composites

BioMed
Research International

Journal of
Metallurgy

Journal of
Materials

Submit your manuscripts at
http://www.hindawi.com

Hindawi

Journal of
Nanoparticles

Advances in
Materials Science and Engineering

Scientifica

Journal of
Nanomaterials

The Scientific
World Journal

International Journal of
Biomaterials

Journal of
Nanoscience

Journal of
Coatings

Journal of
Crystallography

Journal of
Ceramics

Journal of
Textiles